Proceedings of the IASS 2024 Symposium
Redefining the Art of Structural Design
August 26-30, 2024, Zurich Switzerland
Philippe Block, Giulia Boller, Catherine DeWolf,
Jacqueline Pauli, Walter Kaufmann (eds.)

Reconsidering the historical cap ceiling: layerwise form-finding of self-supporting vaulted structures for in situ 3D printing

Frederic CHOVGHI*, David RICHTER[a], Kathrin DÖRFLER[a], Pierluigi D'ACUNTO[b, c]

* Technical University of Munich, TUM School of Engineering and Design, Department of Architecture, Professorship of Structural Design
Arcisstraße 21, 80333 Munich, Germany
frederic.chovghi@tum.de

[a] Technical University of Munich, TUM School of Engineering and Design, Department of Architecture, Professorship of Digital Fabrication, Germany
[b] Technical University of Munich, TUM School of Engineering and Design, Department of Architecture, Professorship of Structural Design, Germany
[c] Technical University of Munich, TUM Institute for Advanced Study (TUM-IAS), Germany

Abstract

Traditional cap ceilings, self-supporting vaulted structures once prevalent in historical masonry construction, are experiencing renewed interest due to their potential for material efficiency and reduced waste. This resurgence comes amidst a pressing need to reduce material consumption in construction. However, the contemporary fabrication of such vaulted structures presents practical challenges. Leveraging advancements in 3D printing, this research seeks to revive cap ceilings by integrating historical techniques with computational structural design and extrusion-based additive manufacturing. Our approach aims to develop a fabrication-aware method for designing formwork-free, self-supporting cap ceiling structures suitable for in situ 3D printing using earthen materials. Using graphic statics, we propose an iterative method for simultaneously form-finding and analyzing the cap ceiling on a global (entire structure) and local (during fabrication) scale. Based on the generated print path, a method for robotic motion planning for cylindrically equivalent target objectives is developed. Physical prototypes using a mobile robot for earth extrusion are fabricated to validate and assess the feasibility of the proposed design and fabrication approach. This interdisciplinary investigation aims to bridge the gap between historical craft and contemporary design and fabrication methods, offering sustainable approaches for future construction practices.

Keywords: cap ceiling, vaulted structures, self-supporting structures, form-finding, graphic statics, Combinatorial Equilibrium Modeling, additive manufacturing, 3D printing of earth, in-situ fabrication

1. Introduction

Due to the relatively low cost of building materials and the higher labor cost, the slab ceiling has prevailed over the historical cap ceiling in contemporary times. However, given the imperative to substantially reduce material consumption across all economic sectors due to climate change, the necessity arises to reconsider this development and the associated construction methods. Constructing cap ceilings with self-supporting masonry layers represents an effective approach to addressing this challenge and offering a viable alternative to the widely used slab ceiling system. Cap ceilings offer highly efficient ceiling structures and prevent waste production during construction due to formwork-free fabrication. However, the lack of skilled masons and the time-consuming fabrication process make historical masonry techniques not readily applicable to the contemporary construction industry [1].

Using contemporary methods like extrusion 3D printing on an architectural scale with earth or concrete enables these techniques to be reinterpreted in the current construction context, as demonstrated by Carneau et al. [2]. This research aims to advance the ongoing work with a method to simultaneously form-find the geometry and print path of the cap ceiling on global and local scales, incorporating iterative structural analysis together with a robotic motion planning approach for extrusion 3D printing of the form-found cap ceiling geometry. Hence, this paper is structured as follows: Starting from the introduction and the research context in Section 1, the research objective is stated in Section 2. The methodological design approach is described in Section 3, and its application is laid out in Section 4. Observations and conclusions can be found in Section 5.

1.1. The historical cap ceiling

The traditional masonry cap ceiling, as shown in Figure 1, is constructed by a series of adjacent caps spanning two lateral beams. It is considered a subtype of the barrel vault. With a cross-sectional curve like a segmental arch, this cap is created by trimming a barrel vault with two vertical planes. The cap was usually fabricated as a halfstone or Catalan vault and could be assembled without formwork [3]. Following Tebbe [4], the cap ceiling can be fabricated, as in the case of the barrel vault [5], with masonry layers rotated 0°, 45° (also called the dovetail bond [5]), and 90° to the longitudinal vault axis. As researched by Aziz et al. [6], the fabrication of the historical masonry cap ceiling offers the possibility to reduce embodied carbon by 50% to comparable slab ceilings made of reinforced concrete. A contemporary reinterpretation of the cap ceiling, wherein the prefabricated cap is composed of rammed earth and spans between two timber beams, was recently proposed by Herzog & de Meuron [7].

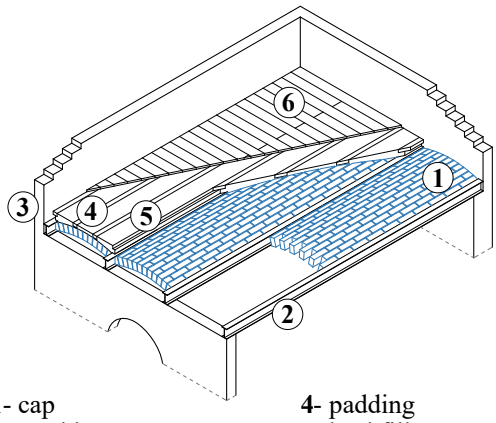

1- cap
2- steel beam
3- massive wall
4- padding
5- backfill
6- flooring

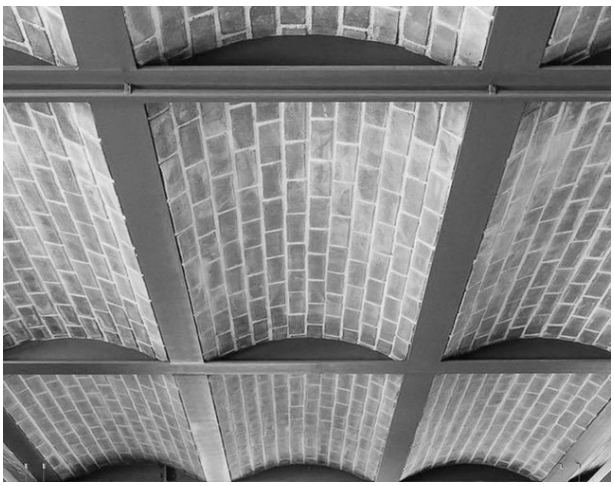

Figure 1: The historical cap ceiling. Left: Construction of the historical masonry ceiling between two steel beams. Massive walls are used as lateral shear supports, and in several historical cases, mineral waste material has been used as backfill [8]. Right: Interior perspective of a capped ceiling construction (photo by Francisco Nogueira, source: https://francisconogueira.com/antonio-costa-lima-junqueira/, accessed: Jun. 27, 2024).

1.2. From masonry to 3D printing

As previously outlined, using cap ceilings nowadays has become increasingly rare, and a direct re-implementation in a contemporary economic context is not practical nowadays. However, recently developed methods for extrusion 3D printing share significant similarities with historical masonry construction and open the possibility of reinterpretation towards automated fabrication [9]. On the one hand, these similarities can be attributed to fabrication-related aspects. In both approaches, the global geometry is generated and significantly influenced by the fabrication process, rooted in a series of repetitive steps like laying a brick stone or extruding a segment of the print path. On the other hand, historical masonry construction and extrusion 3D printing utilize materials with high compressive strength compared to their lower tensile strength. Despite the disparities in corner jointing and composition, the principles of historical masonry construction can thus be transferred to 3D printing [2]. Following the in situ manufacturing methods of its historical predecessors, in 2004, Khoshnevis initially introduced a novel approach by proposing a concept for extrusion-based 3D printing for self-supporting

ceiling systems [10]. This pioneering concept, depicted in Figure 2, featured the utilization of either a gantry system (left) or collaborative mobile robots (right). These systems were designed to fabricate cap ceiling structures directly at their designated location and orientation. However, the mechanical arrangement of each system presents distinct opportunities and limitations for the printing process. Of particular significance to this study are the print direction and sequencing. While gantry systems enable the printing of cap ceilings from above, traversing across supporting beams, mobile robots typically print such caps from below, necessitating aligning the print direction parallel to the support beams. In both cases, these aspects directly affect the process timings, i.e., material hardening and stabilization requirements, and thus, the design and form-finding of the cap geometry.

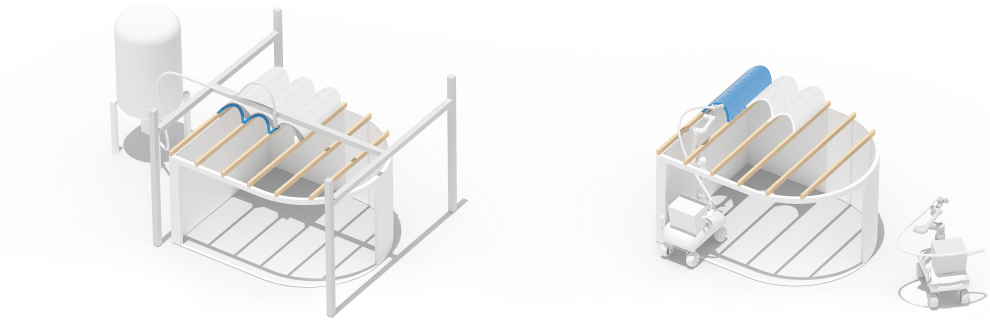

Figure 2: In situ 3D printing strategies. Left: gantry system printing layer by layer from above, with material supplied by a silo. Right: mobile robots printing cap by cap from below. A tank is attached to the robot, providing material.

A form-finding approach for extrusion 3D printing of cantilevers from concrete was presented by Bhooshan et al. [11]. Examples of the reinterpretation process, from the historical vaulting methods to extrusion 3D printing, can be found in the work of Motamedi et al. [12] and Curth et al. [13]. Darweesh and Rael have investigated an on-site 3D earth extrusion approach for fabricating a vaulted structure on an architectural scale [14], and Anton researched the formwork-free fabrication of a 3D-printed Nubian vaulted ceilings made of concrete as lost formwork [15]. In these methods, however, either the global geometry is created initially, and a print path is generated based on this target geometry, or the print path is interpolated directly based on two boundary curves without generating or form-finding the global geometry. These approaches lead to a distinction between global geometry and print path and create direct dependencies, restricting the concurrent control of both in the same hierarchy level. Regarding additive fabrication, examples of vaulted structures printed using stationary systems can be found in [15], and quasi-stationary systems are discussed in [14]. Yet, there are currently no physical examples of mobile robots being used to exceed the early concepts by Khoshnevis in practical applications.

2. Research objective

This research introduces a graphic statics-based method for concurrent form-finding of a 3D printed cap on global (entire structure) and local (during fabrication) scales to control the entire fabrication process of the structure, as initially described in [16]. In the context of this work, global is defined as the final state of the entire geometry and print path, while local is considered as the layer-by-layer state of the geometry and print path during manufacturing, where the layers are considered as fully closed paths. The print path is regarded as a spatial curve that describes the central axis of the print layer. For this purpose, the constraints resulting from extrusion-based 3D printing towards using a mobile robot with print sequencing along the beams are implemented in the design approach together with an adapted structural analysis. Additionally, a robotic motion planning method for the stationary deployment of a 6DOF (degrees of freedom) robotic manipulator for the 3D printing task is developed and integrated into the design approach. This integration aims to enable successful in situ fabrication using a fully mobile robotic setup in the future. Physical prototypes are fabricated to evaluate and calibrate this design method. The overall aim is to develop a material-efficient, 3D printable cap ceiling structure on an architecturally applicable scale.

3. Methodological design approach

As depicted in Figure 3, the global and local state of the geometry and the robotic print path are form-found based on the initial design parameters and the related constraints, described in Section 3.1, concurrently within the same hierarchy level, further explained in Section 3.2. An adapted version of the Combinatorial Equilibrium Modeling method CEM [17], [18], [19] is used for the constraint-driven global and local form-finding. In the subsequent step, the form-found structure is analyzed based on the force transfer, the buckling, and the print layer overhang on a global and local scale in Section 3.3. If the analysis proves the form-found geometry, the robotic motions are generated for fabrication, as explained in Section 3.4. Otherwise, the structure is iteratively optimized until all constraints are fulfilled. A more detailed description of the proposed design approach can be found in [16].

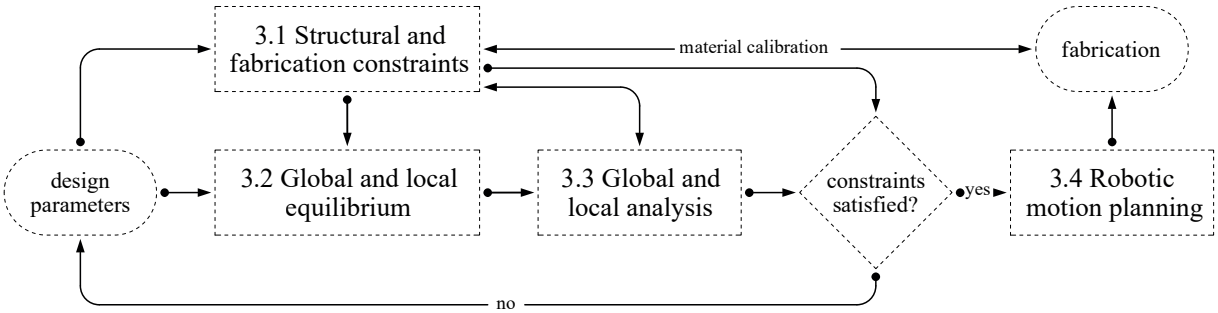

Figure 3: Design workflow for concurrently form-finding the global and local cap with the interdependent print path. A structural analysis and a potential adjustment based on the constraints are additionally embedded. The robotic motions for fabrication are generated if all the defined constraints are fulfilled.

3.1. Design parameters and constraints

In the context of this research, the design parameters are considered as the *span* C_s, the *rise* C_r, and the *length* C_l of the cap. Also, the *tilt angle* a_m of the individual print layers and the *specific weight* γ of the material used for defining the decisive load case in the form-finding step are considered design parameters. The constraints described in Table 1 are categorized into structural and fabrication constraints and, together with the design parameters, form the basis for form-finding.

Table 1: Constraints of the iterative design approach. The constraints restrict the design space on a global and local scale. (a) describes the structural constraints, and (b) outlines the constraints arising from fabrication.

(a) structural constrains		**(b) fabrication constraints**			
BLF_{min}	min buckling load factor	$C_{s,max}$	max span of the cap [mm]	$l_{w,max}$	max layer width [mm]
σ_{min}	min stress [N/mm²]	$C_{r,max}$	max rise of the cap [mm]	$l_{h,min}$	min layer height [mm]
σ_{max}	max stress [N/mm²]	$C_{l,max}$	max length of the cap [mm]	$l_{h,max}$	max layer height [mm]
$l_{o,max}$	max layer overhang [mm]	$l_{w,min}$	min layer width [mm]	$a_{m,max}$	max tilt angle of the layers [°]

3.2. Global and local equilibrium

CEM [17], [18], [19] employs a directed graph as topological diagram ***T*** to generate systemically and control equilibrium states. These infinite equilibrium solutions can be represented as vector-based [20] *form diagram* ***F*** and *force diagram* ***F**, as shown in Figure 4, ***T1***. CEM iteratively computes the nodal equilibrium solution, considering the topological distance of the individual vertices v_i to the supports. The elements with the largest topological distance, defining the starting vertices for equilibrium calculation, are called *origin nodes* $v_{o,i}$. The vertices with the closest topological distance are defined as *support vertices* $v_{s,i}$. *Trail elements* t_{i-j} form the shortest topological path between $v_{o,i}$ and $v_{s,i}$ and are controlled by their length and combinatorial state (tension or compression). *Deviation elements* d_{i-j} interconnect any v_i of the system and are controlled by their force magnitude. [17]

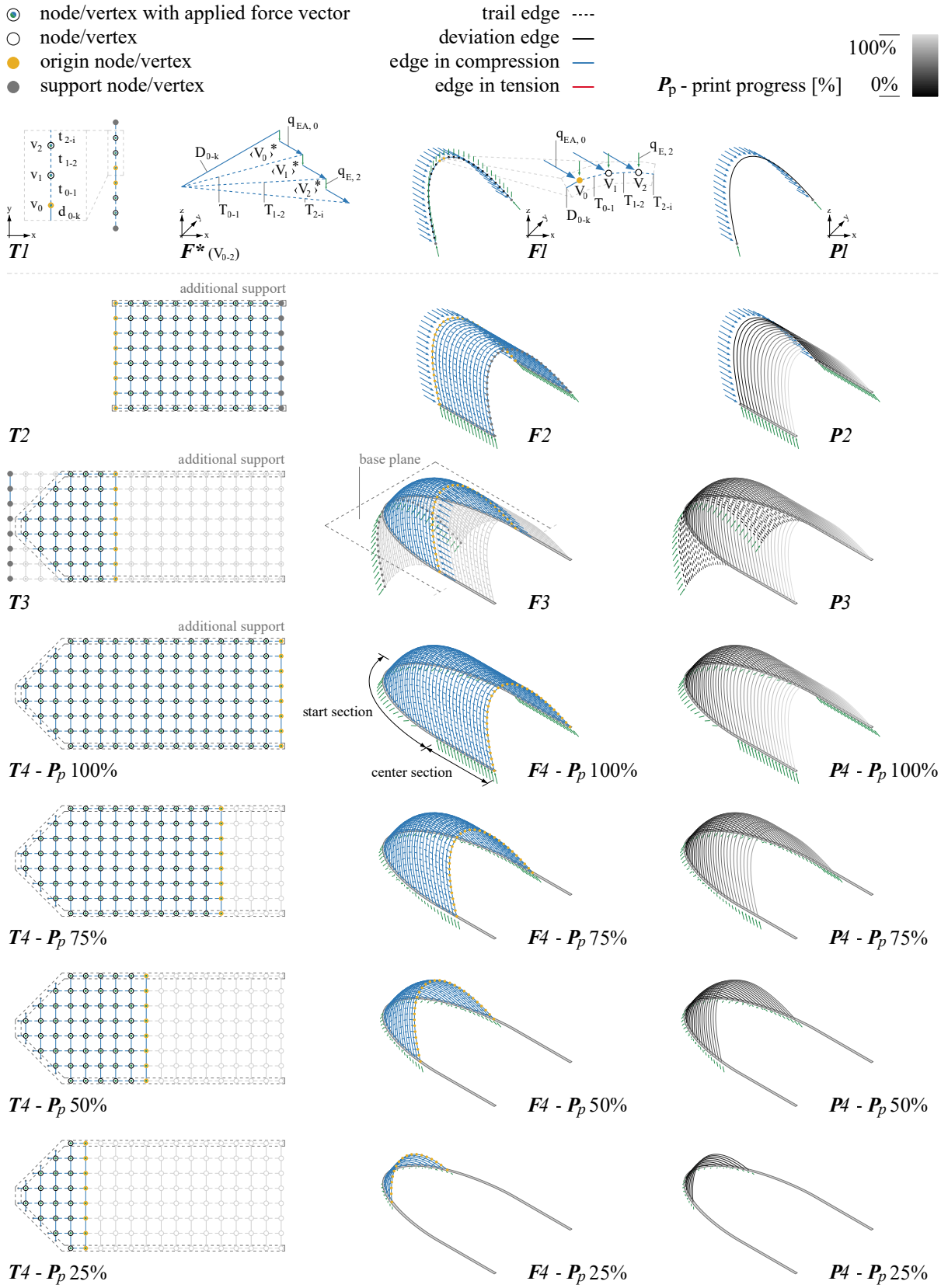

Figure 4: Global (***T1*** – ***T4***, P_p100%) and local form-finding (***T4***, P_p 75% – 25%) of the geometry and the print path of the proposed cap ceiling, based on the method described in Section 3.2. ***T*** represents the topological diagram and is simplified in terms of resolution for readability. ***F*** delineates the resulting form diagram, and ***P*** represents the robotic print path, depending on the print progress P_p.

Using the CEM, an arch representing the cross-section of the main part of the cap is generated. ***T*** is described as two series of trail elements t_{i-j} with a connecting deviation element d_{0-1} between the origin vertices $v_{o,i}$ and $v_{o,j+1}$. The self-weight is considered on a nodal base as a point load in the negative z-direction with a magnitude equal to the weight of the tributary volume of the local print layer. By adjusting the force magnitude of d_{i-j} and the count of t_{i-j}, the curvature of the arch, the span C_s, and the rise C_r of the arch and the subsequent cap are controlled. The magnitude of t_{i-j} is limited to compression. The tilt angle of the arch a_m is implemented by adding auxiliary force vectors $q_{EA,i}$ on every vertex v_i of the system, as shown in Figure 4, ***T1***. An additional optimization loop for setting C_s and C_r to specified values is implemented [17], [18], [19]. The *center section* of the cap ceiling is generated by using the nodes V_i of the initial arch as $V_{o,i}$ and adding a series of t_{i-j}, representing the number of print layers of the center section, together with layerwise interconnecting d_{i-j} elements, as shown in Figure 4, ***T***2. The auxiliary force vectors $q_{EA,i}$ are adjusted accordingly. The length control of t_{i-j} enables the implementation of the layer height. Additional supports are added at the endpoints of the individual arches. By reversing $q_{EA,i}$, and adjusting the force magnitude of d_{i-j}, the *start section* of the cap is constructed following the same design approach in the opposite direction. However, to enable a fabrication with overall constant layer heights, t_{i-j} in ***T*** are increased in resolution until every T_{i-j} intersects with the horizontal base plane. The form diagram ***F*** is trimmed by this base plane, as shown in Figure 4, ***T3***. Combining the two parts and considering the auxiliary force vectors as internal forces generates the global geometry of the cap, as exemplified in Figure 4, ***T4***. Next to this global structure, the local equilibrium condition for every print state, controlled by the print progress $\boldsymbol{P}_p$ [%], is modeled. This enables the control of the structure in the final state and during fabrication. Since the global geometry and the interdependent print path are already generated, the local equilibrium solution, regarded as a local thrust network, should lie within the volume of the global structure. However, as in the case of domes [16], the local equilibrium solution can always be found within this specific global geometric configuration due to the uniform distribution of forces and the persistent tilted layers with constant layer heights. Accordingly, the structure can be modeled in any fabrication state, always considering the individual layers fully closed, as shown in Figure 4, ***T4*** $\boldsymbol{P}_p$ 25%-100%. This allows the precise control of the global and local equilibrium state, enabling the possibility of 3D printing the entire structure only with internal compression forces.

3.3. Global and local analysis

Following the global and local form-finding method, every normal force in any element over the entire fabrication is evaluated and compared with σ_{min}, and σ_{max} to avoid the collapse of the structure. Additionally, a finite element analysis based on Karamba 3D [21] is implemented to evaluate the global and local buckling load factor *BLF* established on a mesh geometry directly generated from the global form diagram ***F***. Since the actual structure-related green state material properties are not assessed yet, default material parameters (clay, medium plastic) are chosen to calculate an initial BLF_{init}. To evaluate the actual minimum BLF_{min}, a series of material calibration prototypes are fabricated to calibrate BLF_{init} with the material properties derived from these tests (BLF_{min} is described as a factor of BLF_{init}). The resultant BLF_{min} is retraced into the structural constraints. Furthermore, the local layer overhang l_o is assessed and restricted within the structural constraint. The maximum layer overhang $l_{o,max}$ refers to the configuration where the projected center of mass for a given print layer precisely falls upon the peripheral boundary of the preceding layer's footprint.

3.4. Robotic motion planning

A method for robotic motion planning is required to transition from the structural design to the fabrication. In motion planning, self-collisions and collisions with the environment and incompatible motion patterns must be avoided to create a valid trajectory. In this study, a mobile robot comprising a 6-axis robot arm mounted on a wheeled mobile base operates in stationary mode, simplifying the motion planning process to focus solely on the movement of the robot arm. The input print path, represented by a curve and a print direction, is extracted directly from the CEM form diagram ***F*** by joining the *deviation elements* D_{i-j}. As depicted in Figure 5, Step 1, every layer of the print path is discretized by *n* target frames (i.e., points with tool orientation).

When printing cap ceiling structures from below with the print direction aligned parallel to support beams, as illustrated in Figure 2, right, the support beams substantially constrain the possible robotic motions. However, in extrusion 3D printing, a round nozzle can rotate around its effective symmetry axis without affecting the print result. Similarly, rotating the initial target frame around the tool axis creates a new equivalent target frame. Repeating this approach, the search space for a valid trajectory can be subdivided progressively to find various robot configurations for this one target (Figure 5, Step 2). For the robotic setup used in this research and described in Section 4.1, most target frames within the length of the robotic arm can be reached from eight different configurations. These configurations are returned by the inverse kinematics equations [22] in the form of joint angles and can include configurations that cause collisions between robot/robot and robot/environment (Figure 5, Step 3).

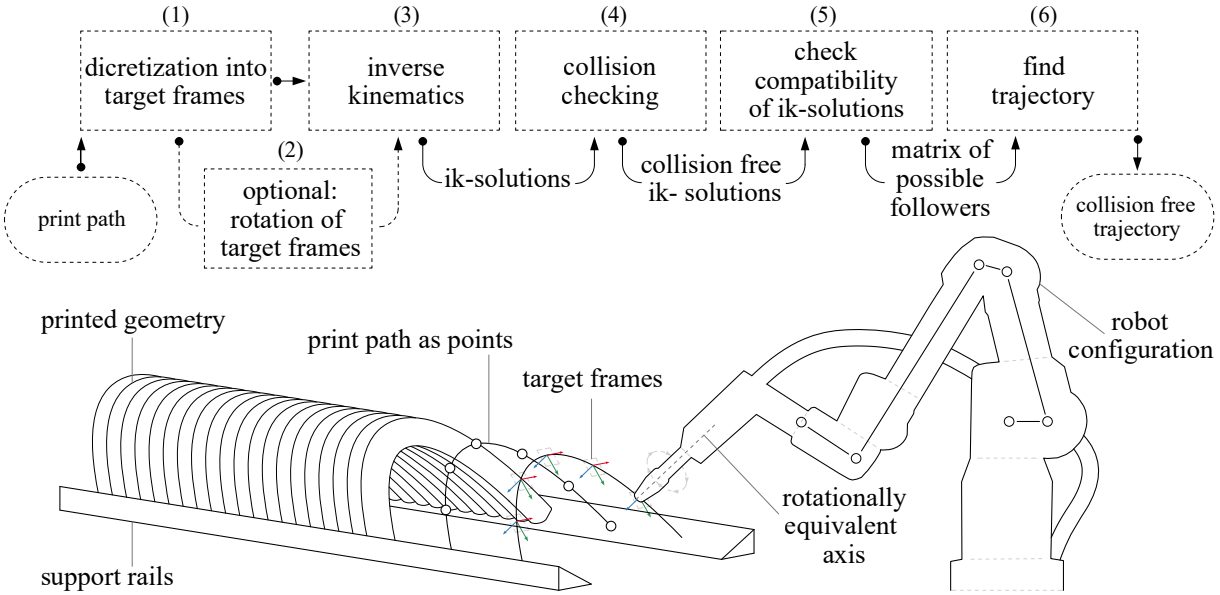

Figure 5: Robotic motion planning. Top: from curves to a valid trajectory in 6 steps. (1) discretization, (2) extending search space by rotating target frames, (3) returning robot configurations for each target frame by solving inverse kinematics, (4) eliminating solutions that result in collisions, (5) checking collision-free configurations for compatibility with neighboring configurations, (6) use compatibility information to create a trajectory. Bottom: toolpath abstraction. The orientation of the tool around its center axis can be determined in the motion planning. Support rails are shown as exemplary collision objects that are accounted for in the motion planning.

Collision checks are performed on a low poly mesh for each configuration to discard invalid solutions (Figure 5, Step 4). To find a valid trajectory, the tool must not deviate from the printpath, particularly when traversing the robot's singularity zone characterized by a fully extended joint. At this singularity, the extended joint rotation in either direction leads to equivalent motion for the tooltip, which can cause jumps in the planned trajectory. To avoid this, solutions are checked for compatibility by ensuring that the square of the difference of all joint angles φ is below a set threshold ε. For every configuration, the compatible configurations of the next point are used to find a valid trajectory to the next target, where the angular deviation across all joints is limited to the set threshold. (Figure 5, Step 5). Reiterating this process for all frames creates a list of segments. Randomly choosing compatible segments yields the final trajectory (Figure 5, Step 6). Choosing the neighboring configuration with the lowest angular change would make the algorithm deterministic but is considered inferior to randomness because, while optimal for this section of the trajectory, it limits the choices on later sections of the trajectory. To optionally minimize the angular change over the entire trajectory and approach an optimum, multiple valid trajectories can be generated and compared.

4. Implementation and results

4.1. Material properties and fabrication setup

An earth material consisting of 32.5% clay, 46.6% sand, 0.81% fibers, and 20.1% water (percentages in relation to specific weight) with a specific weight in green state γ of 23044.00 N/m³ was used for fabricating the caps. The fabrication setup used in this work entails a UR10e robot arm mounted on a Robotnic RB-Vogui XL mobile robotic base. The setup also includes an Ewellix linear lift, which was not used in the experiments. For material transport, an m-tec P20 Connect pump was used with a 5m long, 25mm diameter hose. The hose was connected to a 3D printed nozzle as the tool, with nozzle diameters ranging from 10mm to 22mm. The geometry was printed onto a timber support structure, raising it about 1m above ground level. The specific structural and fabrication constraints described in Table 2 top are evaluated based on this fabrication setup and the design studies shown in Table 2 bottom.

Table 2: Top: Specified structural constraints (a) and fabrication constraints(b) based on the chosen 3D printing setup. Bottom: Extract from the design study series. Both the design parameters and the constraints are varied to identify the restrictions of the potential design space. The bold text indicates when a constraint is not satisfied.

(a) structural constrains		**(b) fabrication constraints**			
BLF_{min}	3.5	$C_{s,max}$	600 mm	$l_{w,max}$	70 mm
σ_{min}	-1.0 N/mm²	$C_{r,max}$	200 mm	$l_{h,min}$	4 mm
σ_{max}	0.0 N/mm²	$C_{l,max}$	1000 mm	$l_{h,max}$	10 mm
$l_{o,max}$	refer to Section 3.3	$l_{w,min}$	15 mm	$a_{m,max}$	70 °

No.	type	printed layers	C_s [mm]	C_r [mm]	C_l [mm]	a_m [°]	l_w [mm]	l_h [mm]	nozzle size [mm]	print speed [mm/s]	n	BLF	$\sigma_{min/max}$ [N/mm²]	l_o [mm]
1	C	29	400	150	168	50	30-40	4.5	10	40	**12**	5.07	-0.01/0	6
2	C	9	400	150	48	50	15-20	4.5	10	80	**12**	**2.41**	-0.01/0	**6**
3	C	23	400	200	134	40	25	4	10	80	**12**	**2.01**	-0.014/0	6.22
4	C	25	400	200	150	40	25	4	10	80	24	**1.97**	-0.014/0	6.22
5	C	25	400	200	150	40	25*	4	10	80	48	**1.97**	-0.014/0	6.22
6	C	48	400	200	292	40	35-45*	4	16	40	48	3.77	-0.014/0	6.22
7	C	23	400	200	115	50	25-30	4	16	60	24	**2.40**	-0.011/0	5.22
8	C	46	400	150	245	50	35*	4	16	50	24	4.72	-0.01/0	5.22
9	C	80	400	150	413	50	35-40	4	16	40	24	4.18	-0.01/0	5.22
10	C+S	84	400	150	428	50	40	4	16	40	24	9.96	-0.19/0	5.22
11	C+S	131	400	150	679	50	40-48	4	16	40	24	7.32	-0.42/0	5.22
12	C	22	500	200	110	50	25	4	16	40	24	**1.92**	-0.012/0	5.22
13	C	59	500	200	302	50	50+	4	16	40	24	4.45	-0.012/0	5.22
14	C+S	66	600	200	679	50	50-55	8	22	40	24	4.69	-0.66/0	10.44
15	C+S	74	600	200	752	50	70+	8	22	30	24	6.65	-0.92	10.44
16	C	3	400	200	21	70	25-30	10	22	50	24	**1.62**	-0.01/0	**10.44**
17	C	29	400	200	292	70	45	10	22	40	24	4.60	-0.01/0	**10.44**

■ Failure during fabrication C Center section of the cap
∗ Data extrapolated S Start section of the cap

4.2. Design studies

Several design studies, shown in Table 2 bottom, varying within the boundaries of the previously described design parameters and constraints, were 3D printed to establish an overview of the relevant parameters for successful fabrication and, thus, to identify the restrictions of the potential design space. The constraints were determined based on these design studies. The critical failure mode during testing was identified as buckling failure. Design study No.11, exemplarily shown during fabrication in Figure 6 top and its final state in Figure 6 bottom, could be successfully printed, although slight deviations from the designed geometry were detected at the top of individual arches due to the layer pressing. In other

tests, this effect led to collapses, especially in those designs with a large layer l_h to l_w ratio. Moreover, material fluctuations were reported to significantly affect the result, as design study No. 14 demonstrates. The change in water content due to the drying of the material over the testing period resulted in a collapse of the cap despite meeting all the predefined constraints.

Figure 6: Design study No.11. Top: fabrication of the cap. Starting from $\boldsymbol{P}_p$ of 25%, every picture shows 25% steps up to the final print on the right side. Bottom: cap after fabrication.

5. Conclusion

In situ 3D printing of earth or concrete enables a reinterpretation of the historical masonry vaulting techniques with self-supporting layers. This research outlines a possible approach to this reinterpretation using the example of the historical cap ceiling. Based on global and local form-finding and the associated structural analysis, pure compression structures are developed layer by layer. The successful fabrication of some of these prototypes using a mobile robot in stationary mode proves this concept. However, further research is needed before direct implementation in actual construction is feasible. Firstly, the material properties need to be accurately determined and controlled to allow for more precise structural analysis, possibly including the effect of layer pressing during printing. In addition, alternative design variations need to be investigated, focusing on creating geometrically more effective structures, such as increasing buckling resistance through a corrugated geometry of the *center section* of the cap. Finally, the potential design space can be drastically extended by implementing the possibility of moving the robot while printing to enable in situ fabrication at full architectural scale.

Acknowledgments

The project was funded by the German Federal Institute for Research on Building, Urban Affairs and Spatial Development on behalf of the Federal Ministry for Housing, Urban Development and Building with funds from the research funding program „Zukunft Bau Forschungsförderung“ under the funding code 10.08.18.7-22.21.

References

[1] M. Motamedi, R. Mesnil, R. Oval, M. Charrier, and O. Baverel, “Scaffold-Free Robotic 3D Printing of a Double-layer Clay Shell,” in *IASS - Annual Symposium of the International Association for Shell and Spatial Structures*, Jan. 2021.

[2] P. Carneau, R. Mesnil, N. Roussel, and O. Baverel, “Additive manufacturing of cantilever - From masonry to concrete 3D printing,” *Autom Constr*, vol. 116, Aug. 2020, doi: 10.1016/j.autcon.2020.103184.

[3] D. Tazehkand, “Zur Erdbebengefährdung des Iran am Beispiel der Stadt Bam – Analyse und Bewertung der verschiedenen Bauweisen und Untersuchung der Kappendecke als wesentliches Bauteil,” Doctoral Thesis, Technische Universität Berlin, Berlin, 2011.

[4] H. Tebbe, “Besonderheiten historischer Bodenaufbauten,” 2010.

[5] D. Wendland, *Lassaulx und der Gewölbebau mit selbsttragenden Mauerschichten. Neumittelalterliche Architektur um 1825-1848*. Imhof Verlag, 2008.

[6] S. Aziz, E. Brechenmacher, B. Alexander, J. Loutfi, and C. Gengnagel, "Cap Ceilings Revisited: A Fabrication Future for a Material-Efficient Historic Ceiling System," in *Design for Rethinking Resources*, 2023, pp. 393–408. doi: 10.1007/978-3-031-36554-6_25.

[7] Herzog & de Meuron, "543 Hortus - Allschwil, Switzerland." Accessed: Apr. 03, 2024. [Online]. Available: https://www.herzogdemeuron.com/projects/543-hortus/

[8] C. Riccabona and K. Mezera, *Baukonstruktionslehre 1*, 9th ed. Manz, 2010.

[9] G. Duarte, N. Brown, A. Memari, and J. P. Duarte, "Learning from historical structures under compression for concrete 3D printing construction," *Journal of Building Engineering*, vol. 43, Nov. 2021, doi: 10.1016/j.jobe.2021.103009.

[10] B. Khoshnevis, "Automated construction by contour crafting—related robotics and information technologies," *Autom Constr*, vol. 13, no. 1, pp. 5–19, Jan. 2004, doi: 10.1016/j.autcon.2003.08.012.

[11] S. Bhooshan, T. Van Mele, and P. Block, "Morph & Slerp," in *Symposium on Computational Fabrication*, ACM, Nov. 2020. doi: 10.1145/3424630.3425413.

[12] M. Motamedi, R. Mesnil, R. Oval, and O. Baverel, "Scaffold-free 3D printing of shells: Introduction to patching grammar," *Autom Constr*, vol. 139, Jul. 2022, doi: 10.1016/j.autcon.2022.104306.

[13] A. Curth, E. G. Alvarez, K. Feickert, C. Mueller, D. M. Schulte, and M. Ismail, "Sueños con tierra/concreto," in *Fabricate 2024*, UCL Press, 2024, pp. 214–221. doi: 10.2307/jj.11374766.31.

[14] B. Darweesh and R. Rael, "From walls to roofs: Formwork-free robotic earthen vault construction," in *Fabricate*, 2024, pp. 40–47.

[15] A.-M. Anton, "Tectonics of Concrete Printed Architecture: Technology, Components and Assemblies for Column-Slab Construction," Doctoral Thesis, ETH Zürich, 2022. doi: 10.3929/ETHZ-B-000605076.

[16] F. Chovghi and P. D'Acunto, "Fabrication-aware structural form-finding for additive manufacturing: An equilibrium-based approach - Under review."

[17] P. O. Ohlbrock and P. D'Acunto, "A Computer-Aided Approach to Equilibrium Design Based on Graphic Statics and Combinatorial Variations," *Computer-Aided Design*, vol. 121, Apr. 2020, doi: 10.1016/j.cad.2019.102802.

[18] R. Pastrana, P. O. Ohlbrock, T. Oberbichler, P. D'Acunto, and S. Parascho, "Constrained Form-Finding of Tension–Compression Structures using Automatic Differentiation," *Computer-Aided Design*, vol. 155, Feb. 2023, doi: 10.1016/j.cad.2022.103435.

[19] P. O. Ohlbrock, P. D'Acunto, J.-P. Jasienski, and C. Fivet, "Constraint-Driven Design with Combinatorial Equilibrium Modelling," in *Proceedings of IASS Annual Symposium*, Aug. 2017.

[20] P. D'Acunto, J.-P. Jasienski, P. O. Ohlbrock, C. Fivet, J. Schwartz, and D. Zastavni, "Vector-based 3D graphic statics: A framework for the design of spatial structures based on the relation between form and forces," *Int J Solids Struct*, vol. 167, pp. 58–70, 2019, doi: https://doi.org/10.1016/j.ijsolstr.2019.02.008.

[21] C. Preisinger and M. Heimrath, "Karamba—A Toolkit for Parametric Structural Design," *Structural Engineering International*, vol. 24, no. 2, pp. 217–221, May 2014, doi: 10.2749/101686614X13830790993483.

[22] R. Rust *et al.*, "COMPAS FAB: Robotic fabrication package for the COMPAS Framework." 2018. doi: 10.5281/zenodo.3469478.